Earth Planet. Sci. Lett. 669 (2025) 119580

Contents lists available at ScienceDirect

Earth and Planetary Science Letters

journal homepage: www.elsevier.com/locate/epsl

Can impact-induced heating drive moderately volatile element loss?

Meredith A. Calogero [a,*], Francis Nimmo [b], Remco C. Hin [a,c]

[a] Bayerisches Geoinstitut, Universität Bayreuth, Bayreuth, Germany
[b] Department of Earth and Planetary Sciences, University of California Santa Cruz, Santa Cruz, USA
[c] Institute of Environmental Geology and Geoengineering, Consiglio Nazionale delle Ricerche (CNR), Milan, Italy

ARTICLE INFO

Editor: O. Mousis

ABSTRACT

Many differentiated planetary bodies are characterised by a depletion in moderately volatile elements (MVEs) and their light isotopes relative to chondrites. We investigate numerically whether hydrodynamic escape of transient atmospheres from planetesimals and planetary embryos in the aftermath of accretional impacts can viably cause this characteristic. Focusing on the case of potassium, we obtain a mass window between about $3 \cdot 10^{21}$ and 10^{23} kg ($5 \cdot 10^{-4}$ to $1.7 \cdot 10^{-2}$ Earth masses) in which hydrodynamic vapour escape is energetically possible. The lower bound most likely arises from inadequate impact energy. The upper bound of 10^{23} kg arises from the gravitational energy precluding escape.

We tracked cumulative impact effects in Grand Tack N-body simulations. Consistent with observations comparing meteorites and terrestrial samples, our simulation results display a lack of correlation between K depletion and body isotopic composition due to mixing of objects with variable K depletion. We find that about one in six bodies that grow beyond 10^{22} kg display significant K loss and isotopic fractionation, and bodies above the maximum loss threshold of $\sim 10^{23}$ kg inherit the depletion signatures from smaller precursors. Our simulations do not produce a correlation between K isotope fractionation and final body mass.

Impact-driven loss may have significantly contributed to MVE depletion among differentiated bodies more massive than $3 \cdot 10^{21}$ kg. If this lower mass bound is not substantially affected by the limitations of the simulation data, then the depletion of smaller objects such as the eucrite parent body must have had a different heat source than impacts, or experienced depletion by a different mechanism than hydrodynamic escape.

1. Introduction

Many silicate and iron achondrites, as well as the bulk silicate Earth and Mars, are characterised by a depletion in moderately volatile elements (MVEs), relative to refractory elements, when compared to chondrites (e.g. O'Neill and Palme, 2008; Hirschmann et al., 2021; Steenstra et al., 2023). Moreover, among the silicate achondrites, many small bodies (e.g. the Moon, 4 Vesta, angrite parent body) are more depleted in such MVEs than the well-characterised planets Mars and Earth, as highlighted, for instance, through K/U and Rb/Sr (e.g. Halliday and Porcelli, 2001; Dauphas et al., 2022). A tight correlation between these element depletions and planetary size is absent, however, because Mars contains higher relative abundances of MVEs than Earth (Dreibus and Wänke, 1985).

This chemical distinction of the, particularly silicate, achondrites from the chondrites is typically attributed to vapour-condensate fractionation. Yet, the cosmochemical setting in which this fractionation occurred remains debated. One hypothesis is that it occurred during gas-dust interaction in the Solar nebula in the same manner that caused the abundances of MVEs to vary among chondrites (e.g. Anders, 1968; Albarède, 2009; Morbidelli et al., 2020). In this case, vapour-condensate fractionation occurs between mineral grains and a gas that likely approximates the Solar photosphere composition, whose conditions are characterised by temperatures $\lesssim 1400$ K (e.g. Lodders, 2003, Wood et al., 2019), low gas pressures ($\lesssim 10^{-3}$ bar), and oxygen fugacities set by the hydrogen-dominant gas (~6 orders of magnitude below the iron-wüstite buffer; $\Delta IW \approx -6$) (e.g. Grossman, 1972). Alternatively, the achondrites could have experienced vapour-condensate fractionation at the surface of their differentiated parent or precursor bodies, with loss of the volatilised material to space (e.g. Urey and Craig, 1953; Ringwood, 1966; Hirschmann et al., 2021). In this planetary setting, relative to the Solar nebula, higher temperatures prevail and pressures may vary from $< 10^{-4}$ to > 10 bar depending on temperature, and the fractionation

* Corresponding author.
E-mail addresses: calogero@umass.edu, Meredith.Calogero@uni-bayreuth.de (M.A. Calogero).

https://doi.org/10.1016/j.epsl.2025.119580
Received 12 February 2025; Received in revised form 4 August 2025; Accepted 7 August 2025

Available online 25 August 2025

likely occurs between silicate (or metal) liquid and vapour at oxygen fugacities $\Delta IW \geq -3$ (e.g. Visscher and Fegley, 2013).

Like the depletion in MVE abundances relative to refractory elements, mass-dependent fractionation of isotopes in silicate achondrites has also been attributed to vapour-condensate fractionation (e.g. Sossi et al., 2016; Hin et al., 2017; Poitrasson et al., 2004; Pringle et al., 2014; Day and Moynier, 2014; Wang and Jacobsen, 2016; Nie and Dauphas, 2019; Fang et al., 2024; Wang et al., 2023). In principle, isotopes have the potential to distinguish between a nebular and planetary vapour-condensate setting, provided that the fractionation occurs between chemically equilibrated vapour and condensates. This trait arises most notably because the isotopes of some elements (e.g. Cr; Sossi and Fegley, 2018) fractionate with a different sign at the oxygen fugacity of a nebular setting compared to that of a planetary setting. Yet, thus far, the isotopic observations seem not to have settled the debate on a cosmochemical setting of fractionation, as they are variably interpreted as occurring in the Solar nebula (e.g. Sossi et al., 2016; Dauphas et al., 2015) or on differentiated planetary bodies (e.g. Day and Moynier, 2014; Pringle et al., 2014).

Three intriguing features have arisen from these isotopic investigations. First, a correlation of isotopic composition with (modern) planetary mass or escape velocity has been presented by Day and Moynier (2014) based on Zn isotopes, the smallest bodies displaying the most fractionated isotopic compositions relative to a terrestrial or chondritic reference. The same observation was made for K isotopes by Tian et al. (2021), the angrite parent body appearing an exception (Hu et al., 2022). This correlation between planetary mass and isotopic fractionation is based on only four planetary objects (Earth, Mars, Moon and Vesta), of which the Moon has a special formation history. At face value, however, a strict dependence of vapour-condensate fractionation on planetary escape velocity suggests that the fractionation occurred at the surface of a planetary body, not in a nebular setting; it is hard to imagine that isotopic fractionation originating from dust-gas interaction in the Solar nebula can remain correlated with escape velocity after accumulating about 20 orders of magnitude of mass (from sub-kg dust to $> 10^{20}$ kg objects) without further fractionation.

Second, isotopic fractionation between vapour and condensate for various elements on the Moon and the depletion of those elements relative to refractory elements is best explained by (near-)equilibrium between the vapour and the condensate (Nie and Dauphas, 2019; Dauphas et al., 2022), as has also been inferred based on theoretical considerations of vaporisation fluxes, free paths of the vaporised molecules and their condensation fluxes (Young et al., 2019; Tang and Young, 2020; Charnoz et al., 2021). This (near-) equilibrium simplifies modelling the effects of vapour-condensate fractionation compared to modelling less constrained disequilibrium processes.

Third, isotopic fractionation has been linked to vapour-condensate fractionation not only for MVEs, but also for the main component elements Fe, Cr, Mg, Si (Poitrasson et al., 2004; Sossi et al., 2016; Pringle et al., 2014; Hin et al., 2017; Young et al., 2019; Zhu et al., 2019; Lu et al., 2024), which are not typically considered as being easily volatilised. The most refractory of these examples is Mg, whose isotopic fractionation may have occurred by evaporative loss of substantial portions of Mg, and hence more volatile elements, from silicate melt at the surfaces of differentiated planetesimals (Hin et al., 2017; Young et al., 2019).

Unlike many preceding studies of vapour-condensate fractionation, the works of Hin et al. (2017) and Young et al. (2019) contain attempts to use physical constraints to quantify the process by which vapour escape could modify the composition of the residual planetary object. The mechanism they propose consists of hydrodynamic escape (Hunten, 1973) of vapour atmospheres coexisting transiently with molten magma at an object's surface. Owing to vigorous convection of the low viscosity, ultra-mafic magmas associated with magma oceans, crusts at the cold surface of a planetesimal are expected to be thin, contain cracks and frequently founder, similarly to lava lakes on Earth (Patrick et al., 2016). This 'open' crust allows for vapour to escape from the magma and to form a (transient) atmosphere that is in chemical equilibrium with the magma below the thin crust (Young et al., 2019; Dauphas et al., 2022; Patrick et al., 2016). Owing to the weak gravity of planetesimals smaller than roughly the size of Mars (Hin et al., 2017), this vapour escapes to space, as opposed to falling back onto the body, leaving behind a residual planetesimal depleted in relatively volatile elements and with fractionated isotopic ratios of these elements.

Young et al. (2019) investigated this scenario with radiogenic decay of ^{26}Al as a heat source for magma oceans, while Hin et al. (2017) focused on the energy deposited by accretional impacts as a potential heat source to produce magma oceans. The model of the latter, however, included a very simple treatment of the conversion of impact energy to internal temperature increases. The temperature of the planetary body is key to quantifying vapour mass loss and consequent chemical changes in the residual body, because it not only determines the presence and temperature of magma, but also the vapour pressure, which greatly influences vapour outflow rates. Here, we focus on improving the model presented in Hin et al. (2017) by including a parameterisation of energy increases in a planetary object based on the work of Nakajima et al. (2021). We explore impact parameter spaces that influence these energy increases and investigate whether vapour loss from impact-induced magma oceans may be relevant in depleting differentiated planetary objects in MVEs.

2. Model

In this study, we model loss and isotopic fractionation of potassium as a consequence of planetesimal impacts during early solar system formation. While our energy balance equations to calculate vapour mass loss can be applied generally, the motivation to focus the chemical part of our modelling on K is two-fold: i) the tight correlation of K isotope compositions with planetary mass observed by Tian et al. (2021), and ii) K is among the more refractory of the MVEs such that the losses and isotopic fractionation obtained in our model may be considered minimum values for the suite of MVEs. The numerical simulations are implemented in the Julia language.

We first use the scaling law relationship developed in Nakajima et al. (2021) to define the energy distribution in a spherical target resulting from impacts for a range of total masses of $0.01 - 1.3 \cdot 10^{23}$ kg, mass ratios of 0.01-0.5 (impact mass versus total mass), and impact velocities of 5-25 km s^{-1} (see section 2.1 for details). We assume the energy increase in the object calculated with Nakajima et al. (2021)'s methods raises its temperature. Using this approach we determine the volume and average initial temperature of the melt, if the temperature rises above the mantle melting point.

For cases where such melting occurs, we incorporate these last two outputs into a thermal model, wherein we track mass loss and geochemical evolution concurrent with cooling of the magma over time. In this thermal model (section 2.2), we solve for evaporative mass loss of a transient atmosphere through hydrodynamic escape (Hin et al., 2017, Young et al., 2019), with its surface vapour pressure determined by the temperature of the molten interior. We assume adiabatic conditions in this atmosphere when determining the mass flux (Zahnle and Catling, 2017), on the basis that the atmosphere is likely convective. The effective surface temperature of the molten body is determined by balancing convective and radiative heat fluxes. The model run proceeds from the initial collision-derived conditions until the interior temperature of the magma ocean decreases to the solidus, set to 1400 K, or the mass loss rate drops to 0 in cases where hydrodynamic escape is no longer energetically possible at temperatures >1400 K, as can be the case for relatively large bodies in our simulations. To calculate the loss of potassium we assume a temperature-dependent melt-vapour partition coefficient (see section 2.3). The isotopic evolution is then tracked assuming an isotopic fractionation factor.

Pre-impact conditions are assumed to be close to the melting point due to early heating by ^{26}Al decay (cf. Nakajima et al., 2021). We do

Table 1
List of parameters used in this study.

Symbol	Description	Value
ρ_B	Bulk Density	3500 kg m^{-3}
ρ_M	Magma Ocean Density	3000 kg m^{-3}
κ	Thermal Diffusivity ($k/\rho_m C_p$)	6×10^{-7} m^2 s^{-1}
ν	Magma Viscosity	1×10^2 Pa s
k	Thermal Conductivity	3 W m^{-1} K^{-1}
C_p	Specific heat capacity	1200 J kg^{-1} K^{-1}
α_V	Thermal Expansivity	$2\cdot10^{-5}$ K^{-1}
L	Latent Heat of Vapourisation	$5\cdot10^6$ J kg^{-1}
M_{mol}	Molar Mass	0.04 kg mol^{-1}
P_v	Surface Vapour Pressure	variable, Pa

not include additional heating associated with ^{26}Al decay in our heat balance model, because the rate of cooling of a molten body (by vapour mass loss and radiation) is several orders of magnitude faster than the rate of heating caused by ^{26}Al decay.

2.1. Conditions of the impact melt

Details regarding our use of the scaling laws of Nakajima et al. (2021) are presented in the Supplementary Information. In brief, we first calculate the distribution of energy gain throughout a body resulting from an impact event. We then use an assumed constant heat capacity (Table 1; Turcotte and Schubert, 2002) of the planetary body to convert the energy gain into a temperature gain relative to an initial temperature, set to 1187 K following Nakajima et al. (2021). The obtained matrix of temperature distributions for a circular grid is then converted into a distribution of melt using peridotite melting points as a function of pressure, following the melting curve of Rubie et al. (2015). Following Nakajima et al. (2021), we assume perfect accretion and model impact angles of $\theta = 0°$, 30°, 45°, 60° and 90°, where a 0° impact is a head-on collision, and a 90° impact grazes the target's surface.

Our results are consistent with those presented in Nakajima et al. (2021) as can be seen in Fig. 1, which presents an example simulation for a total mass equivalent to 1/10th Mars-mass. The 0° and 30° collisions produce global surface melting and a deep molten root below the impact at $\psi = 0°$. The 45° and 60° collisions exhibit global surface melting, with a shallow root in the upper hemisphere. The grazing collision produced only a melt pool local to the impact. We do observe minor antipodal energy gain in all cases, but it is only intense enough to produce a deep molten root during the head-on collision (Fig. 1A,F).

With these results we can compute the volume of melt, V_o, based on the geometry of the melt pool projected onto a sphere, and the volume-averaged temperature of the melt, T_o, based on the average energy increase in regions where melting occurs. We calculate an average temperature for the entire melt volume under the assumption that rapid convection, driven by the sharp temperature drop at the surface of the body, homogenises the temperature of the melt pool. Note that in calculating the temperature, we are neglecting the effect of solid-liquid phase changes and also assuming a constant specific heat capacity, both of which are approximations. We assume the calculated melt volume is spread with uniform thickness over the whole planetary body's surface, to allow our subsequent calculations to be carried out in 1-D. This assumption is consistent with the end-member case examined by Reese and Solomatov (2006) in which post-impact mantle rebound redistributes the melt globally. We provide a breakdown for calculating the volume based on our circular grid in the Supplementary Information.

The quantities V_o and T_o serve as initial conditions for our subsequent numerical work in evaluating a body's potential for loss of atmospheric mass, and elemental and isotopic partitioning into the atmosphere, during cooling after an impact.

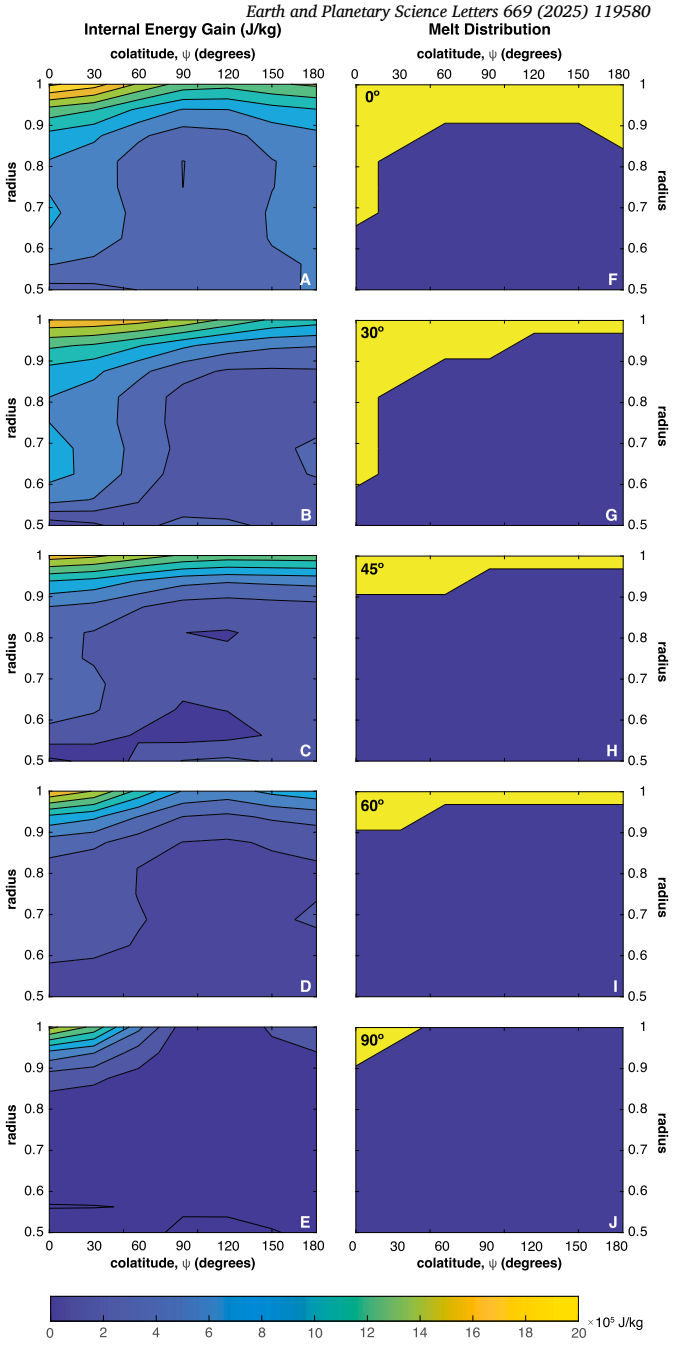

Fig. 1. Internal energy gain (A-E) and melt distribution (F-J) results for various impact angles: (A, F) 0°, (B, G) 30°, (C, H) 45°, (D, I) 60° and (E, J) 90°. All impacts occur at $\psi = 0$, at a velocity of 12 km s^{-1}, involve a sum total mass of $6.4171\cdot10^{22}$ kg ($1/10th$ the mass of Mars) and have an impactor-to-total mass ratio, γ_M, of 0.1. The radial axis is non-dimensionalised, where a radius of 0.5 – 1 represents the core-mantle boundary to the surface. In (F-J), melt is shown in yellow and solid is shown in blue. Partial melt fractions are not considered. These results may be compared with Fig. 8 in Nakajima et al. (2021).

2.2. Thermal evolution

To analyse mass loss from a post-collision planetesimal, we adopt the following physical picture, largely identical to that of Hin et al. (2017). A global magma ocean rapidly produces a transient vapour atmosphere above its surface (Young et al., 2019). It can be demonstrated that the energy required to establish an atmosphere out to the sonic point is a small fraction ($\sim10^{-4}$) of the total thermal energy stored in the magma ocean (see Supplementary Information). The atmosphere is assumed to

be convective and therefore adiabatic. Under some circumstances, the atmosphere is hot and loosely bound enough that vapour loss occurs via radial outflow from the surface, so-called hydrodynamic escape. This mass loss cools the remaining magma, as does direct radiation from the surface of the magma ocean. As the magma cools, the vapour pressure decreases and mass loss declines.

To compute this process, we use T_o obtained above as the initial, internal temperature of the magma ocean. Additional parameters are laid out in Table 1. As in Hin et al. (2017), we solve for the effective surface temperature, T_s, through balancing the radiative loss out of the planetesimal and conduction across the thermal boundary layer at the surface of the convecting magma ocean:

$$T = T_s(1 + T_s^2(\frac{\kappa\nu}{\rho_M g_s \alpha_v})^{1/4}(\frac{2\sigma}{k})^{3/4}) \quad (1)$$

where T is the internal temperature of the magma ocean (when $T(t = 0) = T_o$), κ is thermal diffusivity, ν is magma viscosity, ρ_M is the density of the magma ocean, σ is the Stefan-Boltzmann constant, k is thermal conductivity, α_v is the thermal expansivity of the magma ocean, and g_s is the gravity at the surface of the body: $g_s = (4/3)\pi G\rho_B r$ (G is the gravitational constant, ρ_B is the bulk density and r the planet radius). The heat conducted across the thermal boundary layer is set by the vigour of convection, where here we assume isoviscous convection and obtain the factor of 2 from numerical experiments (Solomatov, 1995). We solve equation (1) by guessing an initial T_s and then iterating. For a body where $T = 1400$ K and $r = 1000$ km, we find $T_s \approx 860$ K, similar to measured temperatures at the surface of terrestrial lava lakes (Patrick et al., 2016).

The internal temperature also allows us to determine the surface vapour pressure (in Pa), P_v, which we determine as in Hin et al. (2017):

$$P_v = 10^5 e^{-4.0041*log(T)^3+88.7878*log(T)^2-639.3032*log(T)+1480.2351} \quad (2)$$

We note that this surface vapour pressure closely matches that of Visscher and Fegley (2013), because it was calibrated against that study.

This surface vapour pressure is set by T and not T_s because we assume that the thin boundary layer is porous and/or fractured enough to allow equilibration of the liquid magma below with the atmosphere above. This assumption is consistent with the lava lake temperatures inferred from gas equilibrium chemistry measurements on Earth (Moussallam et al., 2012). We further use the ideal gas law to calculate the vapour density at the surface, ρ_s:

$$\rho_s = \frac{P_v}{\frac{R}{M_{mol}} * T} \quad (3)$$

where R is the gas constant and M_{mol} is the molar mass of the vapour (Table 1).

We also need to calculate the hydrodynamic mass flux out of our planetesimal, as the vapour mass lost will carry latent heat out of the system, thereby cooling it. For an adiabatic atmosphere, we can follow equation 51 of Zahnle and Catling (2017) to derive the surface outflow velocity, u_s:

$$u_s = c_s\sqrt{2(\frac{\gamma-1}{3\gamma-1}(\frac{\gamma}{\gamma-1} - \frac{GM}{c_s^2 r}))^{\frac{3\gamma-1}{\gamma-1}}(\frac{GM}{4c_s^2 r})^{4\frac{\gamma-1}{3\gamma-1}}(\frac{2}{\gamma})^{\frac{2}{\gamma-1}}} \quad (4)$$

where γ is the adiabatic index, equal to the ratio of specific heat capacities at constant pressure over constant volume (here we take $\gamma = 1.2$ which may be compared with the value of 1.4 for an ideal diatomic gas), M is the total mass of the planetesimal, and c_s is the isothermal sound speed at the surface, derived using the ideal gas law:

$$c_s = \sqrt{\frac{RT}{M_{mol}}}. \quad (5)$$

The surface outflow velocity cannot be negative, so mass loss ceases when u_s drops to 0, and we calculate the mass flux out of the body for $u_s > 0$:

$$\frac{\partial M}{\partial t} = 4\pi r^2 \rho_s u_s \quad (6)$$

The mass flux decreases as cooling proceeds because the surface vapour pressure (equation (2)) decreases as the magma ocean cools. Flow velocities and mass fluxes also decrease with increasing γ, other things being equal (Zahnle and Kasting, 1986).

Based on Zahnle and Kasting (1986) we can also define a critical mass, M_c, above which hydrodynamic escape is energetically not possible:

$$M_c = \left[\frac{\gamma}{\gamma-1}\frac{RT}{GM_{mol}}(\frac{3}{4\pi\rho_B})^{\frac{1}{3}}\right]^{\frac{3}{2}} \quad (7)$$

This expression can also be derived by setting $u_s = 0$ in equation (4). The critical mass is strongly temperature dependent, such that for a body with internal temperature 3000 or 1500 K the critical masses are approximately $1.1 \cdot 10^{23}$ or $3.9 \cdot 10^{22}$ kg, respectively (assuming $M_{mol} = 0.04$ kg mol^{-1}). Attempting to evaluate loss on a body where $M > M_c$ would result in a negative u_s from Equation (4).

We evaluate the rate of cooling of the magma ocean interior as follows:

$$\frac{\partial T}{\partial t} = \frac{\frac{\partial M}{\partial t}(\frac{GM}{r} + L) + \sigma T_s^4 4\pi r^2}{M_l C_p}. \quad (8)$$

The first term in the numerator is the advective term, and shows how mass loss transports latent heat L, and also produces changes in the gravitational potential energy of the body (see Hin et al., 2017). The second term describes radiative heat loss from the planetesimal surface. M_l is the mass of the magma ocean, which decreases over time. We vary the length of each time-step, Δt, over the course of the simulation such that one step forward in time results in one degree of cooling. We assume an emissivity of 1, but a reduction to 0.8 (as a proxy for a grey atmosphere) results in minimal increases in mass loss and subsequent geochemical fractionation (e.g. mass loss increases by about 0.12–0.04%, with smaller increases at higher initial masses).

2.3. Evaporation and fractionation

We address the partitioning of potassium into the transient atmosphere above a cooling magma ocean, as well as its isotopic fractionation, with mass balance equations using a partition coefficient between vapour and liquid ($D^{v/l}$) and an isotopic fractionation factor ($\alpha^{v/l}$). The details of these mass balance equations are presented in the Supplementary Information. We use a partition coefficient based on the output of the thermodynamic vapour-liquid code of Hin et al. (2017) ($1.14 < D^{v/l} < 50$ for 1400 K$< T <$2500 K and $D^{v/l}(T \geq 2500\text{ K}) = 50$). The code of Hin et al. (2017) does not explicitly account for oxygen fugacity, which affects species volatility and hence our K partition coefficient, but comparison to Seidler et al. (2024) implies that our $D^{v/l}$ are relevant for ΔIW$\approx +1$ (see Supplementary Information for details). The equilibrium fractionation factor of K isotopes between (ultra-)mafic silicate liquid and silicate vapour is currently unknown. In this study, we therefore empirically estimate a fractionation factor, for which we consider that the correlation between K isotopes and body mass in Tian et al. (2021) is largely determined by the eucrite parent body (EPB) and Mars, whose masses furthermore closely approach the mass range we model here. We thus use the δ^{41} K difference measured between them of about 0.7 (Tian et al. (2021) and references therein) and the factor of about 2.5 depletion in potassium of the EPB relative to Mars, i.e. $f = 0.21$ (Humayun and Clayton, 1995) to come to an α of 0.999541, assuming a Rayleigh distillation process. We note that equilibrium isotopic fractionation factors are inversely proportional to the square of temperature and hence vary during cooling. However, the (average) temperature of fractionation between the EPB and Mars is unknown, and is it uncertain that this fractionation is entirely due to vapour-condensate fractionation or whether it reflects equilibrium. Combined with the lack of appropriate

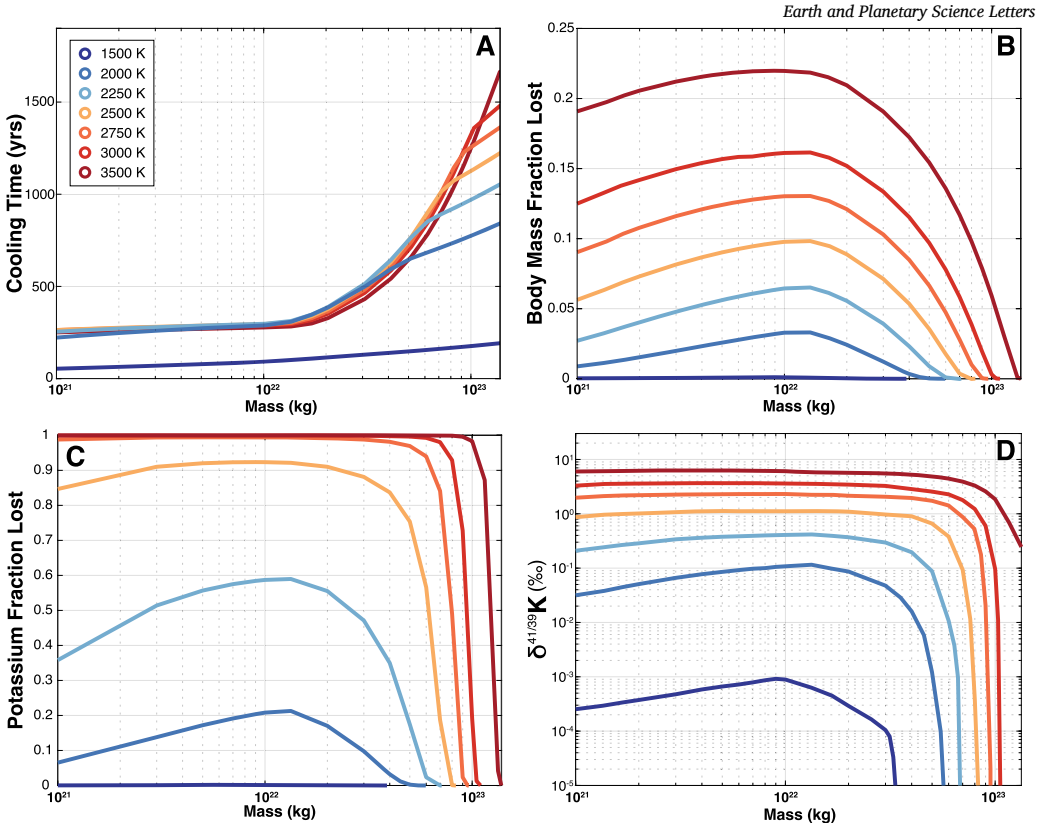

Fig. 2. Results of hydrodynamic escape simulations with imposed initial temperatures and melt volumes. A) Cooling time in years for a range of initial total masses ($0.01–1.333 \cdot 10^{23}$ kg) and temperatures. Coloured curves refer to different initial temperatures (here: synthetic models rather than temperature values derived from impact energy simulations). Cooling and loss were considered complete when the body's internal temperature dropped to 1400 K. B) Body mass fraction lost. C) Potassium fraction lost. D) Final δ^{41} K value.

$\alpha(T)$ available in literature, there is no strong justification for imposing a temperature dependence on our empirical approximation of α.

An effect that we have so far neglected is chemical diffusion. For a motionless layer evaporating a species such as K into space, a K-depleted layer will develop at the surface. In order for subsequent K to reach the surface, it first has to diffuse across the depleted layer. The time for a species to diffuse across a layer of thickness d is given by $\sim\sqrt{\kappa_c t}$ where t is the time elapsed and κ_c is the chemical diffusivity. The rate of K loss from the surface is thus limited by the diffusivity, and presents a potentially serious barrier to evaporation (e.g. Zhang and Driscoll, 2025).

However, the extent to which these micro-scale processes apply to macro-scale magma oceans is unclear. Laboratory-scale experiments of evaporation from molten drops variably display the presence or absence of such diffusion-limited effects, depending e.g. on temperature and evaporation rates relative to diffusion rates (e.g. Sossi et al., 2019; Young et al., 2022, Zhang et al., 2021). The chemistry of gases above terrestrial lava lakes indicates that the gases last equilibrated with the lavas at the actual lava temperatures (e.g. Gerlach, 1980; Moussallam et al., 2012). If solid-state diffusion through a surficial layer had played a role, different species with different diffusivities would have resulted in an apparent equilibrium temperature not consistent with the actual lava temperature. However, an additional complicating factor is that in terrestrial lava lakes, gas loss is controlled by bubble formation. Given the conflicting nature of the evidence, we do not pursue the role of either diffusion limitations or bubble formation here, but suggest that these should be regarded as important issues for future work. The calculated K loss and isotopic fractionation presented in this study should thus represent an upper limit.

3. Results

We first explored how varying the initial temperature of a magma ocean on different-sized bodies affects the extent of mass lost as vapour, and consequent K loss and K isotope fractionation. These simulations are simplified in that they assume an initial temperature and melt volume rather than solving for these quantities based on the impact energy. The results are presented in Fig. 2 for total body masses of $0.01 - 1.3 \cdot 10^{23}$ kg and initial temperatures ranging from 1500 to 3500 K. Here, the entire mantle is assumed to be molten. We report results for M_{mol} of 0.04 kg mol^{-1} unless stated otherwise.

At 1500 K, too little vapour is produced for its loss to influence the cooling regime and, irrespective of body mass, cooling rates are determined by radiative heat loss (Fig. 2A). Because of the strongly non-linear dependence of radiated heat on temperature, the total cooling time is controlled by the lowest temperatures and is not very sensitive to the initial temperature. Above 2000 K vapour mass loss significantly contributes to cooling. For bodies with masses $< 1–2 \cdot 10^{22}$ kg, however, mass loss is so fast that radiative heat loss remains the rate-limiting factor. With further increases in mass, the vapour outflow is the rate-limiting factor, with shorter cooling times for higher initial temperatures due to higher mass flow rates. When vapour outflow becomes inhibited by gravity, cooling occurs again dominantly by radiation, as displayed by the temperature-dependent flattening of curves at high masses in Fig. 2A.

Fig. 2B shows that higher initial temperatures lead to more extensive mass loss. This result in itself is unsurprising, but for each initial temperature there is a notable peak in mass loss for initial masses around $1.3 \cdot 10^{22}$ kg, the highest mass where cooling is primarily restricted by radiation fluxes. For smaller masses, the relatively high surface area:volume ratio imposes a rapid cooling rate (Fig. 2A), so the magma ocean cools quickly and less material is lost overall. In contrast, for bodies

more massive than $1.3 \cdot 10^{22}$ kg the body's gravitational acceleration progressively hinders mass loss by hydrodynamic escape and shuts it off entirely above a critical mass that increases with increasing initial temperature (see equation (7)).

In Fig. 2C we look at the proportion of potassium lost over the same range of initial conditions. Bodies at high initial temperatures (e.g. initial T > 2750 K) lose virtually all of their potassium if the total mass is $< 3 \cdot 10^{22}$ kg. A $1.3 \cdot 10^{22}$ kg body will experience up to approximately $20-90\%$ loss for an initial temperature range of $2000-2500$ K. For bodies more massive than $5 \cdot 10^{22}$ kg, the influence of mass and temperature becomes more important, and a small change in either mass or temperature can be the difference between complete loss or total retention of potassium.

We show the isotopic fractionation of K (δ^{41} K, in permil, with an initial value of 0) in Fig. 2D. We obtain δ^{41} K values >1‰ at masses in the range $4 \cdot 10^{22} - 1.1 \cdot 10^{23}$ kg for initial temperatures of $2500-3500$ K. As anticipated from the results for K loss (Fig. 2C), for increasing mass (e.g. $>5 \cdot 10^{22}$ kg) there is a large change from large to small K isotopic fractionation over a narrow mass interval. We additionally report results with a lower M_{mol} of 0.02 kg mol^{-1} in Fig. S3, and note lower mass and K loss, and lower isotopic fractionation for masses $\lessapprox 2 \cdot 10^{22}$ kg (this arises because of the reduced vapour density, equation (3)). Reduced M_{mol} allows for loss and fractionation from slightly larger body masses than for our baseline model (equation (7)).

3.1. Impact models

Following this simplified exploration of parameter space, we next use our impact calculations (Fig. 1) to investigate the effects on potassium loss and isotopic fractionation of a range of impact velocities (v_{imp}, $5-25$ km s^{-1}), total masses (M_T, $0.01-6 \cdot 10^{23}$ kg) and impactor:total mass ratios (γ_M, $0.01-0.5$). All of these factors play a role in determining the energy generation and distribution in the post-collision body, which controls, to first order, the magma ocean geometry (Nakajima et al., 2021). We performed 9702 simulations over this parameter space, where we either fixed total mass at 1, 5 or $8 \cdot 10^{22}$ kg (Fig. 3), or γ_M (ratio of impactor mass over the total mass) at 0.03, 0.1 or 0.5 (Fig. 4). All simulated impacts had an impact angle of 45°.

In Fig. 3A we show the extent of K loss after cooling for collisions where the total system mass is $1 \cdot 10^{22}$ kg ($M_t + M_i$). We find that collisions need an impact velocity >14 km s^{-1} (or $11.3 \cdot v_{esc}$) when $\gamma_M = 0.5$ to produce enough energy for potassium loss. There is a trade-off between γ_M and impact velocities, but we find vapour mass loss does not occur for $\gamma_M \leq 0.05$, even if v_{imp} reaches 25 km s^{-1} (here, when $M_i < 6 \cdot 10^{20}$ kg). Fig. 3B shows the change in δ^{41} K corresponding to the potassium losses presented in Fig. 3A.

We show K loss in Figs. 3C and E (and corresponding δ^{41} K in panels D and F) for collisions involving total system masses of 5 and $8 \cdot 10^{22}$ kg, respectively. Here, greyed-out regions are those for which the calculated temperature exceeds 3500 K, beyond which silicate liquid is no longer stable and our very simplified temperature calculations are expected to break down. For a total mass of $5 \cdot 10^{22}$ kg, at $\gamma_M = 0.3$, partial K loss occurs when impact velocities are between 10.5 and 14.5 km s^{-1} (5.0 and $6.9 \cdot v_{esc}$ respectively). At the same γ_M, for a total mass of $8 \cdot 10^{22}$ kg, partial K loss is achieved over a more constrained range of v_{imp}, from 11.3 to 13.8 km s^{-1} (equivalent to 4.6 and $5.6 \cdot v_{esc}$).

In Fig. 4 we show simulations for impact scenarios with total system masses ranging from $0.01 - 6 \cdot 10^{23}$ kg and the same impact velocity range of $5-25$ km s^{-1}, while investigating various fixed γ_M. When $\gamma_M = 0.03$ (Fig. 4 A-B), we find only a small range of total masses between $2-9 \cdot 10^{22}$ kg where, at high impact velocities (> 21 km s^{-1}), any potassium loss (< 20%) and change in δ^{41} K value (< 0.3) should be expected.

When $\gamma_M = 0.1$ (Fig. 4 C-D), the minimum impact velocity where we observe any K loss (or change in δ^{41} K value) is roughly 12 km s^{-1}, where the total system mass is approximately $5 \cdot 10^{22}$ kg. When $\gamma_M = 0.1$, at our maximum v_{imp} (25 km s^{-1}), the minimum total mass where we observe K loss is about $6 \cdot 10^{21}$ kg (700 km radius).

When $\gamma_M = 0.5$ (Fig. 4 E-F), the local minimum impact velocity where we observe any K loss (or change in δ^{41} K value) is centred around ≈ 7.25 km s^{-1} with a corresponding mass of $4.5 \cdot 10^{22}$ kg. Note that the minimum impact velocity yielding K loss occurs at a mass that is very similar to that for $\gamma_M = 0.1$, and that both these masses fall in the range of masses with an impact velocity minimum for K loss if $\gamma_M = 0.03$. We highlight the local minimum in each fixed γ_M case with a red tick on the vertical axes of Fig. 4 A,C,E. This mass correspondence is not coincidental; it is related to the interplay between increased cooling rates for higher surface-to-volume ratios at decreasing masses and stronger retention by gravity at increasing masses, just as with the peak losses at $1.3 \cdot 10^{22}$ kg observed in the simplified models shown in Fig. 2. The slight disagreement between the peaks found in Fig. 4 and our simplified calculations presented in Fig. 2 is most likely due to the fact that in the latter the total melt volume is independent of initial temperature while in the former the two quantities are correlated. The lack of dependence of the local minimum on γ_M is due to the fact that escape is controlled by the final system mass (equation (7)). At our maximum v_{imp} (25 km s^{-1}) and γ_M (0.5), mass loss does not occur below about $3 \cdot 10^{21}$ kg.

To evaluate whether actual impacts are likely to cause partial or complete K loss, we show individual impacts from N-body Grand Tack simulations by Carter et al. (2015) as blue dots in Figs. 3 and 4, again assuming all 45° impact angles. These simulations track the collisional evolution of planetesimals distributed over a 2.5 AU radial distance with a total mass of 4.85 Earth masses and individual masses as small as 1.2×10^{20} kg. Jupiter's inwards-then-outwards migration excites the eccentricities of the planetesimals, leading to a burst of collisions at high impact velocities.

A summary of the outcomes of these individual collisions is provided in Table 2. For each of the six scenarios addressed above, we indicate the total number of relevant impacts, out of the study's 37239 impact events. We note the proportion of impacts for each scenario which produce isotopic fractionation values (δ^{41} K) exceeding 0.05‰, this value having been selected because it is a limit above which differences in K isotopic ratios may be analytically resolvable (note that in a simple Rayleigh distillation scenario, 0.05‰ K isotope fractionation corresponds to about 6% K loss if α is 0.999541). For the fixed mass cases, the largest proportion of impacts which caused loss occurred when the total system mass was around $5 \cdot 10^{22}$ kg (4.8%), which is also the mass at which the impact velocity required to induce mass loss is minimised (Fig. 4). We find that the frequency of loss-inducing impacts increases with increasing γ_M.

Of all impacts from the N-body study, 484 (1.4%) involved enough energy to form a magma ocean, and 182 of them (0.5% of all impacts, 37.6% of magma ocean forming impacts) would have resulted in significant potassium loss due to hydrodynamic escape during cooling.

4. Discussion

Our exploration of parameter spaces suggests that, under certain conditions, vapour mass loss can occur on planetary objects, involving K losses that are a strong function of body mass, γ_M or impact velocity. Within the parameter space investigated here, such vapour mass loss is practically absent for impacts where the total mass involved is smaller than $3 \cdot 10^{21}$ kg, even for impact velocities and impactor-to-total mass ratios as high as 25 km s^{-1} and 0.5 (Fig. 4). Similarly, an upper mass bound appears at $\approx 10^{23}$ kg. These two mass thresholds are energy limitations. Impacts at lower masses apparently provide insufficient energy to increase the temperature of the object above the melting point of the silicate mantle. Above the upper mass bound, insufficient energy is available for vapour to escape from the strong gravity.

As indicated in Table 2, in the N-body simulations only 0.5% of all impacts result in measurable loss (i.e. >0.05‰ K isotope fractionation).

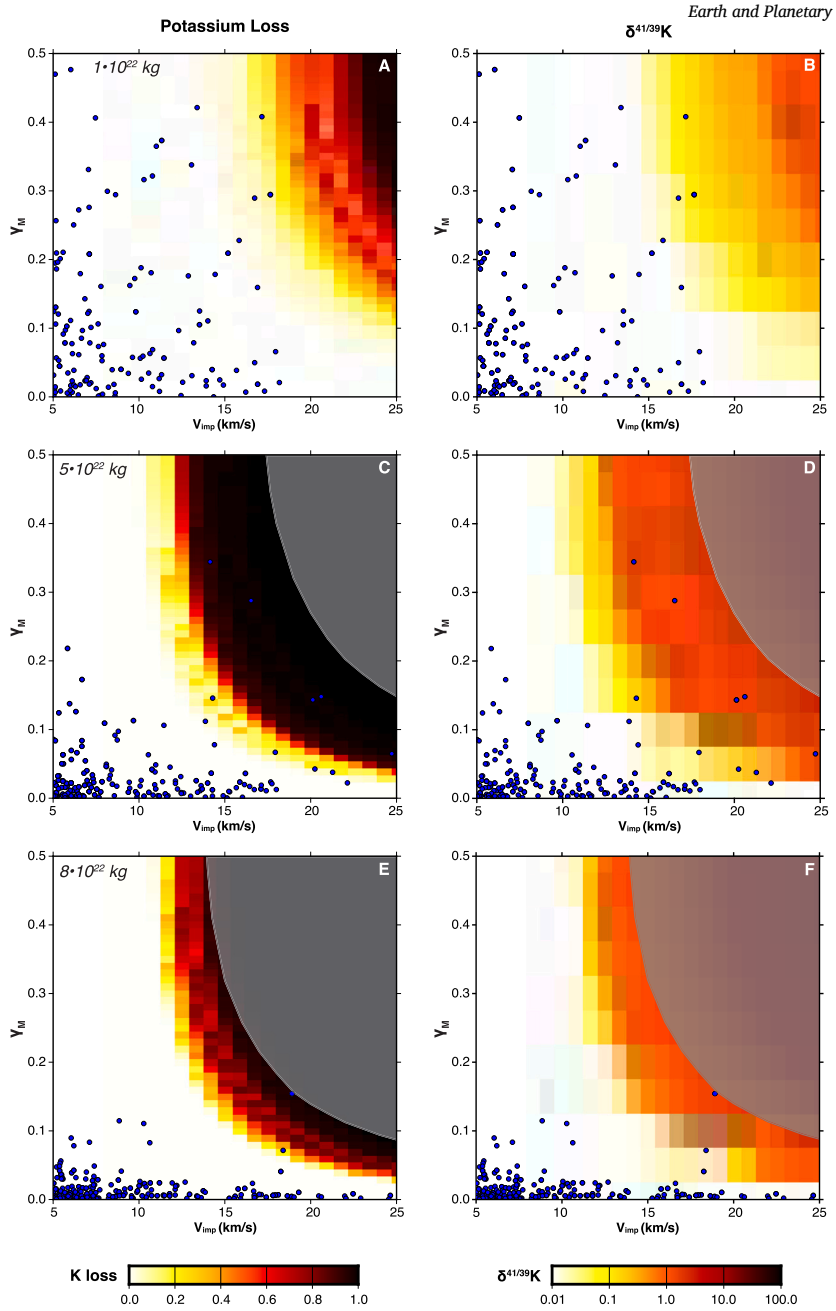

Fig. 3. Potassium fraction lost (panels A, C, E) and isotopic fractionation (B, D, F) for impacts with fixed total masses. Simulation results are for $M_T = 1 \cdot 10^{22}$ kg (A, B), $5 \cdot 10^{22}$ kg (C, D) and $8 \cdot 10^{22}$ kg (E, F). Contour plots are each based on data compiled from 1092 simulations exploring various γ_M and v_{imp}. Where the field is white, no loss is expected, and impacts under conditions where the field saturates to black would result in complete loss of K. Greyed-out regions are where the calculated temperature exceeds 3500 K and our results are not expected to be valid. Blue dots represent impacts from N-body Grand Tack simulations by Carter et al. (2015) for impacts with a fixed total mass from $0.8–1.2 \cdot 10^{22}$ kg (A, B), $4–6 \cdot 10^{22}$ kg (C, D) and $6.4–9.6 \cdot 10^{22}$ kg (E, F).

At face value, this small fraction suggests vapour mass loss by outflow from magma oceans generated by impacts likely played a negligible role in the depletion of moderately volatile elements that is seen in many differentiated planetary bodies (e.g. O'Neill and Palme, 2008).

So far, however, we have evaluated vapour mass losses in the aftermath of a single impact, while planetary objects grow by accretion of mass in multiple impact events. We therefore evaluate the cumulative effects of multiple impacts on the final K loss and isotopic fractionation of a planetary body. As these effects are difficult to predict *a priori*, we identified bodies in N-body simulations by Carter et al. (2015) that experienced multiple impacts, of which at least one impact led to significant vapour mass loss (i.e. >0.05‰ K isotope fractionation). Of the 3246 bodies remaining at the end of the N-body simulations, 3.8% (125 bodies) matched this criterion. This value is smaller than the 182 individual impacts causing significant vapour mass loss (see section 3), implying that cumulative effects indeed occur. In fact, of all 1186 bodies at the end of the N-body simulations that reached a mass higher than $3 \cdot 10^{21}$ kg, 8% (97 bodies) display >0.05‰ K isotope fractionation. Of the 408 bodies surpassing 10^{22} kg, this climbs to 16% (66 bodies), and for the 168 bodies surpassing $3 \cdot 10^{22}$ kg, 18.5% (31 bodies) experience significant K isotope fractionation. Of the 71 bodies present at the end of the N-body simulation who surpassed 10^{23} kg, 5 of them (7%) showed significant K isotope fractionation.

Hence, our simulations predict that about one in six planetary bodies that grow beyond a mass of 10^{22} kg will experience hydrodynamic loss of a significant fraction of its K as vapour due to impact-induced

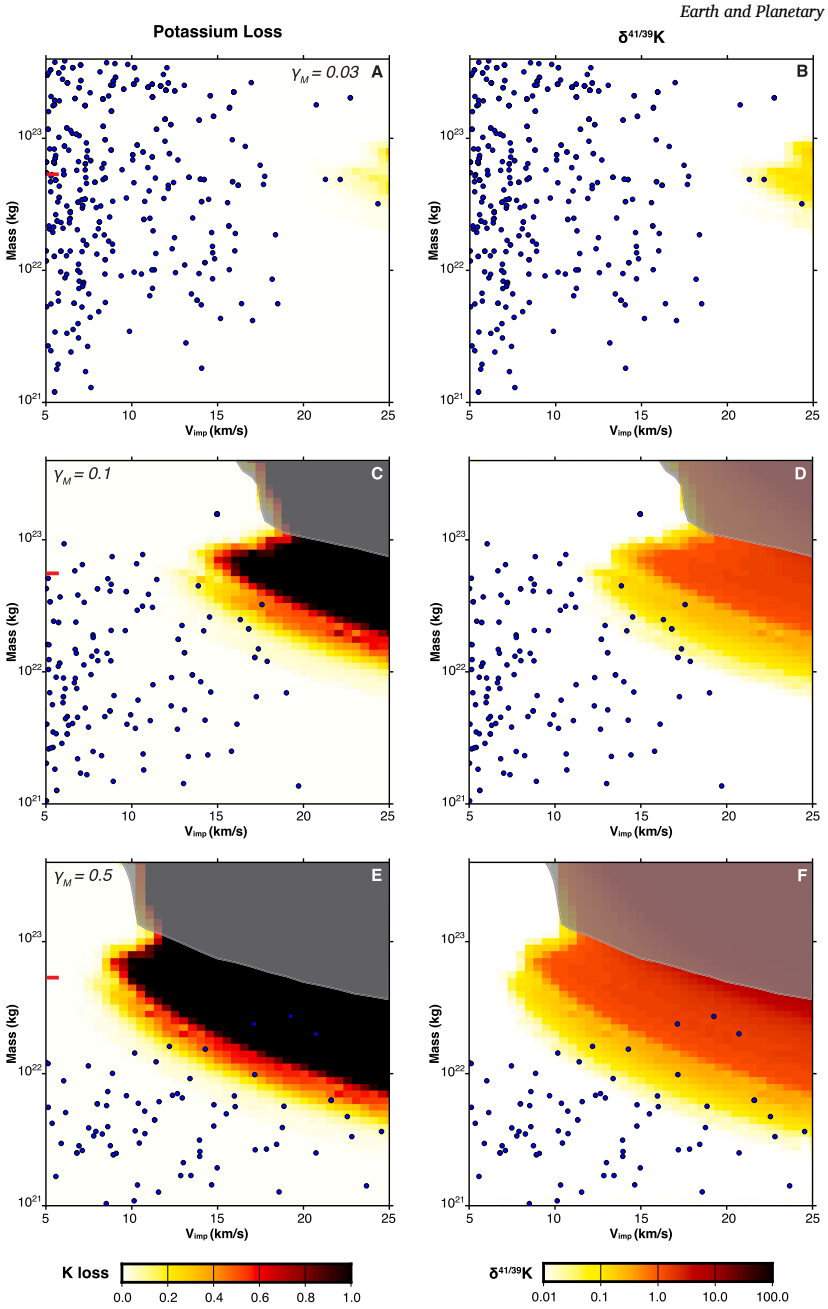

Fig. 4. Potassium fraction lost (panels A, C, E) and isotopic fractionation (B, D, F) for impacts with fixed impactor-to-total mass ratios. Simulation results are for $\gamma_M = 0.03$ (A, B), 0.1 (C, D) and 0.5 (E, F). Each contour plot is based on data compiled from 2142 simulations exploring various M_T and v_{imp}. Where the field is white, no loss is expected. Fields saturated black represent conditions where impacts result in complete loss of K. Greyed-out regions are where the calculated temperature exceeds 3500 K and our results are not expected to be valid. Blue dots are impacts from N-body Grand Tack simulations by Carter et al. (2015), for impacts with γ_M from 0.02–0.04 (A, B), 0.08–0.12 (C, D) and 0.4–0.5 (E, F). Red tick marks on the mass axis (A, C, E) indicate the mass where the impact velocity necessary to induce K loss is minimised.

magma oceans. An evaluation of loss at the high mass end ($> 10^{23}$ kg) is hindered by the small number of bodies and the limited duration of bombardment in the N-body simulations of Carter et al. (2015), making it difficult to get a good sense of average mass loss because of the statistics of small numbers. Nonetheless, as K is one of the more refractory elements among the moderately volatiles, this process of vapour loss may have played a substantial role in the volatile depletion of differentiated bodies that grew to $\gtrsim 5 \cdot 10^{-4}$ Earth masses.

This mechanism of volatile depletion is likely characterised by relatively oxidising conditions (e.g., $\Delta IW \approx -1$), as the oxygen fugacity of the magma ocean-vapour atmosphere system would be set by the oxygen fugacity of the silicate portion of a planetary object (Wolf et al., 2023; Fegley and Cameron, 1987; Visscher and Fegley, 2013). This oxygen fugacity is typically at least three orders of magnitude higher than in the canonical Solar nebula, although the effect of the presence of a H_2-dominated (residual) primordial nebula remains to be investigated. Importantly, depletion of MVEs and concomitant isotopic fractionation under such oxidising conditions is required to explain Cr isotope fractionation on the EPB and the Moon (Zhu et al., 2019) as well as Mn/Na systematics in these objects and similar ones (O'Neill and Palme, 2008).

To further investigate the consequences of cumulative effects by multiple impacts during planetary growth, in Fig. 5 (and Table S5) we present the K isotope fractionation and the K remaining in 88 of the final bodies that experienced at least one loss event. In presenting these

Table 2
Isotopic fractionation of K in single impact events occurring in Grand Tack simulations of Carter et al. (2015), as graphically represented by blue dots in Figs. 3 and 4. Percentages refer to the total number of impacts with measurable isotopic fractionation of K relative to the total number of impacts with each mass or γ_M initial condition. Note that there is overlap in the datasets between the two scenarios.

M_T (kg)	γ_M	Total Impacts	δ^{41} K> 0.05	%
$1 \cdot 10^{22}$	-	150	3	2.0%
$5 \cdot 10^{22}$	-	210	10	4.8%
$8 \cdot 10^{22}$	-	330	2	0.6%
-	0.03	365	3	0.8%
-	0.1	136	9	6.6%
-	0.5	79	15	19.0%

results, chondrites rich in K are arguably the best reference point, but their K isotope compositions are variable and, in some cases, debated (Wang and Jacobsen, 2016; Ku and Jacobsen, 2020). Since our main goals here are merely to investigate the potential consequences of cumulative effects on an object's K abundance, we instead chose the K abundance and isotopic composition of Mars as initial composition for our simulations, which is within an order of magnitude scale in mass relative to the largest bodies resulting from the N-body simulations.

Fig. 5A reveals that the relation between K isotope fractionation and K loss predicted by Rayleigh fractionation is only followed by bodies that experienced a loss event that was not followed by any later mass addition. Conversely, bodies that experienced a single vapour mass loss event followed by later mass addition as well as nearly all bodies that experienced multiple loss events followed by later mass addition fall off this Rayleigh fractionation prediction. In other words, mixing of different bodies with variable K (isotope) depletion breaks down the correlation between mass loss and isotopic fractionation that is dictated by the simple dependence of the latter on the former, effectively dampening the isotopic fractionation effect and causing the scatter seen in Fig. 5A.

This scatter predicted by our simulations is, in fact, observed in nature for K isotopes in the differentiated planetary bodies and in chondrites (Bloom et al., 2020; Tian et al., 2021; Nie et al., 2023). These observations and our simulations thus imply that caution should be exercised in drawing conclusions regarding fractionation processes based on the relative abundances of an element compared to their isotopic composition.

Contrary to the lack of correlation between K/U (a proxy for K loss) and K isotope composition for multiple planetary objects, Tian et al. (2021) highlighted a tight correlation (R^2 of 0.998) between K isotope composition and the body masses of Earth, Mars, the Moon and the eucrite parent body, the K isotope ratios of the Earth and Mars being similar to that of enstatite chondrites. This correlation could be fortuitous, but Tian et al. (2021) suggested it may also exist for Rb isotopes, while Day and Moynier (2014) have previously highlighted it in Zn isotopes. The angrite parent body is a notable outlier to this correlation, as it appears enriched in light rather than heavy isotopes relative to chondrites (at least for K and Rb; Hu et al., 2022; Wang et al., 2023).

Tian et al. (2021) proposed that the correlation they observed may indicate that K isotope fractionation was dominantly created in K vapour loss events that occurred at/near the final mass of the planetary object. This hypothesis, however, is hard to reconcile with the extreme difficulty in losing volatile elements from bodies as large as Mars or the Earth (equation (7) and Fig. 2).

Alternatively, mixing of bodies variably depleted in K (isotopes) has been proposed as cause for this correlation (Sossi et al., 2022). No correlation between isotopic fractionation and mass is revealed, however, in Fig. 5B. Part of the reason for this absence may simply be that very few bodies experience mass loss below $\sim 10^{22}$ kg and none at all below $3 \cdot 10^{21}$ kg. As explained above, this result arises because a minimum impact energy (and thus target mass) is required to create a magma ocean and subsequent hydrodynamic escape during cooling. The N-body data that we used arise from simulations that do not allow for appearance of new, low mass bodies after the start of a simulation, which likely occurs (Lichtenberg et al., 2021). Therefore, few bodies smaller than 10^{21} kg are present when the Grand Tack excites impacts to maximum velocities exceeding 25 km s^{-1}. This simulation characteristic may skew our minimum mass threshold, which needs to be tested in future work. If this threshold does not require significant modification, however, then hydrodynamic escape of vapour from impact-induced magma oceans cannot explain the isotopic fractionation and moderately volatile element depletion in bodies smaller than $3 \cdot 10^{21}$ kg, such as the eucrite parent body. Whether ^{26}Al decay is capable of driving such escape (Young et al., 2019) is debatable as its heating rate is orders of magnitude smaller than cooling rates of molten bodies (cf. Fig. 2 for cooling rates). It may be that for small bodies a different mechanism than the one investigated here may have contributed to MVE depletion and isotopic fractionation. The implication of a correlation between body mass and isotopic fractionation, however, is that this mechanism is still likely to be vapour-condensate fractionation on planetary bodies. This conundrum remains a topic of investigation.

4.1. Future work

The Nakajima et al. (2021) parameterisation that we use is the best currently available, but its treatment of melt production is simplified. Our approach makes additional simplifications in calculating the mean magma ocean temperature. While the qualitative behaviour is unlikely to change, both the vapour pressure and the mass limit beyond which escape is shut off (equation (7)) depend on the temperature assumed. A more complete thermodynamic treatment of this problem would be desirable, as are N-body simulations that allow for appearance of new, low mass objects during the evolution of a planetary disk.

As noted in Section 2.3, the role of bubble formation and/or diffusion has been neglected in this work. The extent to which these micro-scale processes are relevant to macro-scale magma oceans is currently unclear, but may well be important and should be the focus of future work.

5. Conclusions

In this work we have explored the potential for large impacts to drive loss and fractionation of a moderately volatile element, potassium, via hydrodynamic escape. The results may be summarised as follows. First, for the expected impact velocities K loss is negligible in systems with masses less than 3×10^{21} kg (roughly 600 km radius) (Fig. 4). This is a consequence of insufficient energy delivery. Second, mass loss is most efficient at masses close to 10^{23} kg (radius about 2000 km) and falls off sharply at higher masses (Fig. 4), because escape velocities exceed any likely thermal velocity. Potassium loss from Mars- or Earth-mass bodies is expected to be negligible. Third, we used the accretion simulations of Carter et al. (2015) to investigate how much K loss is expected for bodies which experience multiple impacts in a dynamically-excited system. In these simulations, bodies with final masses $< 3 \times 10^{21}$ kg experienced negligible loss, but about one in six of the bodies $> 10^{22}$ kg experienced measurable potassium loss. These bodies did not show a correlation between final mass and isotopic fractionation, because of the overprinting effects of late impacts bringing in potassium without significant loss. Impact-driven loss is thus potentially an important process for embryo-sized bodies, but appears unable to explain the depletion in MVEs in smaller bodies such as the eucrite parent body. Whether loss driven by ^{26}Al heating is a viable mechanism remains to be seen; alternatively, explaining volatile depletion on planetesimals appears to require a process that to our knowledge is currently not understood.

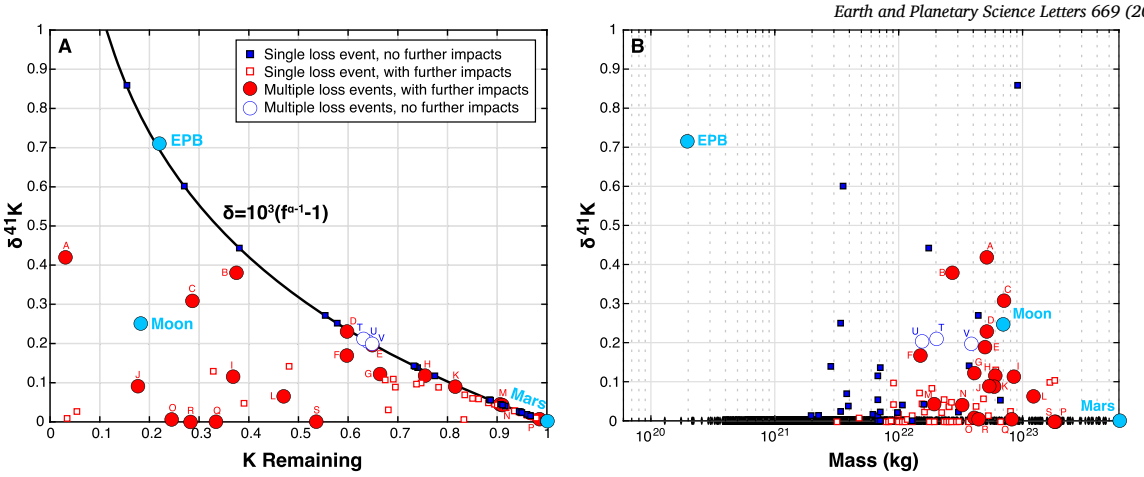

Fig. 5. Cumulative effects of vapour mass loss on final bodies during their growth history with multiple impact events as recorded by N-body simulations (Carter et al., 2015). Letters correspond with impact series data reported in Table S5. A) Final K fraction remaining vs δ^{41} K fractionation. B) Final total body mass vs δ^{41} K fractionation. In each panel, squares represent 66 bodies whose impact growth series included only one event where our model predicts K loss. Circles are 22 bodies whose impact series included multiple such events. Dark blue are series where the final impact (or multiple impacts) were the one(s) where loss is predicted. Red are the series where, after impact(s) where loss is predicted, further impacts occurred where we do not predict loss. Light blue circles show values from Dauphas et al. (2022) for the eucrite parent body, the Moon and Mars. The black curve in panel A) shows the expectations from Rayleigh fractionation. Black dots in panel B show the distribution of final masses from the remaining 3159 bodies from the N-body Grand Tack simulations that did not experience any significant K isotope fractionation.

CRediT authorship contribution statement

Meredith A. Calogero: Writing – review & editing, Writing – original draft, Visualization, Software, Methodology, Investigation, Formal analysis, Data curation. **Francis Nimmo:** Writing – review & editing, Writing – original draft, Visualization, Validation, Supervision, Methodology, Investigation, Formal analysis, Data curation. **Remco C. Hin:** Writing – review & editing, Writing – original draft, Validation, Supervision, Resources, Project administration, Funding acquisition, Formal analysis, Conceptualization.

Declaration of competing interest

The authors declare that they have no known competing financial interests or personal relationships that could have appeared to influence the work reported in this paper.

Acknowledgements

This work was funded by ERC Starting Grant 949417 Vaploss. FN acknowledges support from NASA-80NSSC21K0388. We thank Paolo A. Sossi and Nicole X. Nie for insightful reviews that helped improve this manuscript, and Olivier Mousis for editorial support.

Appendix A. Supplementary material

Supplementary material related to this article can be found online at https://doi.org/10.1016/j.epsl.2025.119580.

Data availability

Data will be made available on request.

References

Albarède, F., 2009. Volatile accretion history of terrestrial planets and dynamic implications. Nature 461, 1227–1233. https://doi.org/10.1038/nature08477.

Anders, E., 1968. Chemical processes in the early solar system, as inferred from meteorites. Acc. Chem. Res. 1 (10), 289–298. https://doi.org/10.1021/ar50010a001.

Bloom, H., Lodders, K., Chen, H., Zhao, C., Tian, Z., Koefoed, P., Pető, M.K., Jiang, Y., Wang, K., 2020. Potassium isotope compositions of carbonaceous and ordinary chondrites: implications on the origin of volatile depletion in the early solar system. Geochim. Cosmochim. Acta 277, 111–131. https://doi.org/10.1016/j.gca.2020.03.018.

Carter, P.J., Leinhardt, Z.M., Elliott, T., Walter, M.J., Stewart, S.T., 2015. Compositional evolution during rocky protoplanet accretion. Astrophys. J. 813 (1), 72. https://doi.org/10.1088/0004-637x/813/1/72.

Charnoz, S., Sossi, P.A., Lee, Y.-N., Siebert, J., Hyodo, R., Allibert, L., Pignatale, F.C., Landeau, M., Oza, A.V., Moynier, F., 2021. Tidal pull of the Earth strips the proto-moon of its volatiles. Icarus 364, 114451. https://doi.org/10.1016/j.icarus.2021.114451.

Dauphas, N., Poitrasson, F., Burkhardt, C., Kobayashi, H., Kurosawa, K., 2015. Planetary and meteoritic Mg/Si and δ^{30}Si variations inherited from solar nebula chemistry. Earth Planet. Sci. Lett. 427, 236–248. https://doi.org/10.1016/j.epsl.2015.07.008.

Dauphas, N., Nie, N., Blanchard, M., Zhang, Z., Zeng, H., Hu, J., Méheut, M., Visscher, C., Canup, R., Hopp, T., 2022. The extent, nature, and origin of K and Rb depletions and isotopic fractionations in Earth, the Moon, and other planetary bodies. Planet. Sci. J. 3, 29. https://doi.org/10.3847/PSJ/ac2e09.

Day, J., Moynier, F., 2014. Evaporative fractionation of volatile stable isotopes and their bearing on the origin of the Moon. Philos. Trans. R. Soc., Math. Phys. Eng. Sci. 372. https://doi.org/10.1098/rsta.2013.0259.

Dreibus, G., Wänke, H., 1985. Mars, a volatile-rich planet. Meteoritics 20 (2).

Fang, L., Moynier, F., Barrat, J.-A., Yamaguchi, A., Paquet, M., Chaussidon, M., 2024. The origin of 4-Vesta's volatile depletion revealed by the zinc isotopic composition of diogenites. Sci. Adv. 10 (33), eadl1007. https://doi.org/10.1126/sciadv.adl1007.

Fegley, B., Cameron, A., 1987. A vaporization model for iron/silicate fractionation in the Mercury protoplanet. Earth Planet. Sci. Lett. 82 (3), 207–222. https://doi.org/10.1016/0012-821X(87)90196-8.

Gerlach, T., 1980. Evaluation of volcanic gas analyses from Kilauea volcano. J. Volcanol. Geotherm. Res. 7 (3–4), 295–317.

Grossman, L., 1972. Condensation in the primitive solar nebula. Geochim. Cosmochim. Acta 36 (5), 597–619. https://doi.org/10.1016/0016-7037(72)90078-6.

Halliday, A., Porcelli, D., 2001. In search of lost planets – the paleocosmochemistry of the inner solar system. Earth Planet. Sci. Lett. 192 (4), 545–559. https://doi.org/10.1016/S0012-821X(01)00479-4.

Hin, R., Coath, C., Carter, P.J., Nimmo, F., Lai, Y.J., von Strandmann, P. Pogge, Willbold, M., Leinhardt, Z.M., Walter, M.J., Elliott, T., 2017. Magnesium isotope evidence that accretional vapour loss shapes planetary compositions. Nature 549, 511–515. https://doi.org/10.1038/nature23899.

Hirschmann, M.M., Bergin, E.A., Blake, G.A., Ciesla, F.J., Li, J., 2021. Early volatile depletion on planetesimals inferred from C–S systematics of iron meteorite parent bodies. Proc. Natl. Acad. Sci. USA 118 (13), e2026779118. https://doi.org/10.1073/pnas.2026779118.

Hu, Y., Moynier, F., Bizzarro, M., 2022. Potassium isotope heterogeneity in the early Solar System controlled by extensive evaporation and partial recondensation. Nat. Commun. 13, 7669. https://doi.org/10.1038/s41467-022-35362-7.

Humayun, M., Clayton, R.N., 1995. Potassium isotope cosmochemistry: genetic implications of volatile element depletion. Geochim. Cosmochim. Acta 59 (10), 2131–2148. https://doi.org/10.1016/0016-7037(95)00132-8.

Hunten, D.M., 1973. The escape of light gases from planetary atmospheres. J. Atmos. Sci. 30 (8), 1481–1494. https://doi.org/10.1175/1520-0469(1973)030<1481:TEOLGF>2.0.CO;2.

Ku, Y., Jacobsen, S.B., 2020. Potassium isotope anomalies in meteorites inherited from the protosolar molecular cloud. Sci. Adv. 6 (41), eabd0511. https://doi.org/10.1126/sciadv.abd0511.

Lichtenberg, T., Draçźkowska, J., Schönbächler, M., Golabek, G.J., Hands, T.O., 2021. Bifurcation of planetary building blocks during solar system formation. Science 371 (6527), 365–370.

Lodders, K., 2003. Solar system abundances and condensation temperatures of the elements. Astrophys. J. 591 (2), 1220. https://doi.org/10.1086/375492.

Lu, W., Weber, R., Zhang, Z., Li, Y., 2024. Experimental determination of Si, Mg, and Ca isotope fractionation during enstatite melt evaporation. Am. Mineral. 109 (7), 1193–1202. https://doi.org/10.2138/am-2023-9111.

Morbidelli, A., Libourel, G., Palme, H., Jacobson, S., Rubie, D., 2020. Subsolar Al/Si and Mg/Si ratios of non-carbonaceous chondrites reveal planetesimal formation during early condensation in the protoplanetary disk. Earth Planet. Sci. Lett. 538, 116220. https://doi.org/10.1016/j.epsl.2020.116220.

Moussallam, Y., Oppenheimer, C., Aiuppa, A., Giudice, G., Moussallam, M., Kyle, P., 2012. Hydrogen emissions from Erebus volcano, Antarctica. Bull. Volcanol. 74, 2109–2120.

Nakajima, M., Golabek, G.J., Wünnemann, K., Rubie, D.C., Burger, C., Melosh, H.J., Jacobson, S.A., Manske, L., Hull, S.D., 2021. Scaling laws for the geometry of an impact-induced magma ocean. Earth Planet. Sci. Lett. 568, 116983. https://doi.org/10.1016/j.epsl.2021.116983.

Nie, N.X., Dauphas, N., 2019. Vapor drainage in the protolunar disk as the cause for the depletion in volatile elements of the moon. Astrophys. J. Lett. 884 (2), L48. https://doi.org/10.3847/2041-8213/ab4a16.

Nie, N.X., Chen, X.-Y., Zhang, Z.J., Hu, J.Y., Liu, W., Tissot, F.L., Teng, F.-Z., Shahar, A., Dauphas, N., 2023. Rubidium and potassium isotopic variations in chondrites and Mars: accretion signatures and planetary overprints. Geochim. Cosmochim. Acta 344, 207–229. https://doi.org/10.1016/j.gca.2023.01.004.

O'Neill, H., Palme, H., 2008. Collisional erosion and the non-chondritic composition of the terrestrial planets. Philos. Trans. R. Soc., Math. Phys. Eng. Sci. 366, 4205–4238. https://doi.org/10.1098/rsta.2008.0111.

Patrick, M., Orr, T., Swanson, D., Lev, E., 2016. Shallow and deep controls on lava lake surface motion at Kīlauea Volcano. J. Volcanol. Geotherm. Res. 328. https://doi.org/10.1016/j.jvolgeores.2016.11.010.

Poitrasson, F., Halliday, A.N., Lee, D.-C., Levasseur, S., Teutsch, N., 2004. Iron isotope differences between Earth, Moon, Mars and Vesta as possible records of contrasted accretion mechanisms. Earth Planet. Sci. Lett. 223 (3), 253–266. https://doi.org/10.1016/j.epsl.2004.04.032.

Pringle, E.A., Moynier, F., Savage, P.S., Badro, J., Barrat, J.-A., 2014. Silicon isotopes in angrites and volatile loss in planetesimals. Proc. Natl. Acad. Sci. USA 111 (48), 17029–17032. https://doi.org/10.1073/pnas.1418889111.

Reese, C., Solomatov, V., 2006. Fluid dynamics of local martian magma oceans. Icarus 184 (1), 102–120. https://doi.org/10.1016/j.icarus.2006.04.008.

Ringwood, A., 1966. Chemical evolution of the terrestrial planets. Geochim. Cosmochim. Acta 30 (1), 41–104. https://doi.org/10.1016/0016-7037(66)90090-1.

Rubie, D., Jacobson, S., Morbidelli, A., O'Brien, D., Young, E., de Vries, J., Nimmo, F., Palme, H., Frost, D., 2015. Accretion and differentiation of the terrestrial planets with implications for the compositions of early-formed Solar System bodies and accretion of water. Icarus 248, 89–108. https://doi.org/10.1016/j.icarus.2014.10.015.

Seidler, F.L., Sossi, P.A., Grimm, S.L., 2024. Impact of oxygen fugacity on the atmospheric structure and emission spectra of ultra-hot rocky exoplanets. Astron. Astrophys. 691, A159.

Solomatov, V.S., 1995. Scaling of temperature- and stress-dependent viscosity convection. Phys. Fluids 7 (2), 266–274. https://doi.org/10.1063/1.868624.

Sossi, P., Stotz, I., Jacobson, S., Morbidelli, A., O'Neill, H., 2022. Stochastic accretion of the Earth. Nat. Astron. 6, 1–10. https://doi.org/10.1038/s41550-022-01702-2.

Sossi, P.A., Fegley, Bruce Jr., 2018. Thermodynamics of element volatility and its application to planetary processes. Rev. Mineral. Geochem. 84 (1), 393–459. https://doi.org/10.2138/rmg.2018.84.11.

Sossi, P.A., Nebel, O., Anand, M., Poitrasson, F., 2016. On the iron isotope composition of Mars and volatile depletion in the terrestrial planets. Earth Planet. Sci. Lett. 449, 360–371. https://doi.org/10.1016/j.epsl.2016.05.030.

Sossi, P.A., Klemme, S., O'Neill, H.S.C., Berndt, J., Moynier, F., 2019. Evaporation of moderately volatile elements from silicate melts: experiments and theory. Geochim. Cosmochim. Acta 260, 204–231.

Steenstra, E., Renggli, C., Berndt, J., Klemme, S., 2023. Evaporation of moderately volatile elements from metal and sulfide melts: implications for volatile element abundances in magmatic iron meteorites. Earth Planet. Sci. Lett. 622, 118406. https://doi.org/10.1016/j.epsl.2023.118406.

Tang, H., Young, E.D., 2020. Evaporation from the lunar magma ocean was not the mechanism for fractionation of the Moon's moderately volatile elements. Planet. Sci. J. 1 (2), 49. https://doi.org/10.3847/PSJ/abb23c.

Tian, Z., Magna, T., Day, J.M.D., Mezger, K., Scherer, E.E., Lodders, K., Hin, R.C., Koefoed, P., Bloom, H., Wang, K., 2021. Potassium isotope composition of Mars reveals a mechanism of planetary volatile retention. Proc. Natl. Acad. Sci. USA 118 (39), e2101155118. https://doi.org/10.1073/pnas.2101155118.

Turcotte, D.L., Schubert, G., 2002. Geodynamics. Cambridge University Press.

Urey, H.C., Craig, H., 1953. The composition of the stone meteorites and the origin of the meteorites. Geochim. Cosmochim. Acta 4 (1), 36–82. https://doi.org/10.1016/0016-7037(53)90064-7.

Visscher, C., Fegley, J., 2013. Chemistry of impact-generated silicate melt-vapor debris disks. Astrophys. J. Lett. 767, L12. https://doi.org/10.1088/2041-8205/767/1/L12.

Wang, B., Moynier, F., Hu, Y., 2023. Rubidium isotopic compositions of angrites controlled by extensive evaporation and partial recondensation. Proc. Natl. Acad. Sci. USA 121. https://doi.org/10.1073/pnas.2311402121.

Wang, K., Jacobsen, S., 2016. Potassium isotopic evidence for a high-energy giant impact origin of the Moon. Nature 538, 487–490.

Wolf, A., Jäggi, N., Sossi, P., Bower, D., 2023. VapoRock: thermodynamics of vaporized silicate melts for modeling volcanic outgassing and magma ocean atmospheres. Astrophys. J. 947, 64. https://doi.org/10.3847/1538-4357/acbcc7.

Wood, B.J., Smythe, D.J., Harrison, T., 2019. The condensation temperatures of the elements: a reappraisal. Am. Mineral. 104 (6), 844–856. https://doi.org/10.2138/am-2019-6852CCBY.

Young, E., Shahar, A., Nimmo, F., Schlichting, H., Schauble, E., Tang, H., Labidi, J., 2019. Near-equilibrium isotope fractionation during planetesimal evaporation. Icarus 323, 1–15. https://doi.org/10.1016/j.icarus.2019.01.012.

Young, E.D., Macris, C.A., Tang, H., Hogan, A.A., Shollenberger, Q.R., 2022. Isotope velocimetry: experimental and theoretical demonstration of the potential importance of gas flow for isotope fractionation during evaporation of protoplanetary material. Earth Planet. Sci. Lett. 589, 117575.

Zahnle, K.J., Catling, D.C., 2017. The cosmic shoreline: the evidence that escape determines which planets have atmospheres, and what this may mean for Proxima Centauri B. Astrophys. J. 843 (2), 122. https://doi.org/10.3847/1538-4357/aa7846.

Zahnle, K.J., Kasting, J.F., 1986. Mass fractionation during transonic escape and implications for loss of water from Mars and Venus. Icarus 68 (3), 462–480. https://doi.org/10.1016/0019-1035(86)90051-5.

Zhang, Z., Driscoll, P.E., 2025. Inefficient loss of moderately volatile elements from exposed planetesimal magma oceans. J. Geophys. Res. Planets 130 (2), e2024JE008671. https://doi.org/10.1029/2024JE008671.

Zhang, Z.J., Nie, N.X., Mendybaev, R.A., Liu, M.-C., Hu, J.J., Hopp, T., Alp, E.E., Lavina, B., Bullock, E.S., McKeegan, K.D., et al., 2021. Loss and isotopic fractionation of alkali elements during diffusion-limited evaporation from Molten silicate: theory and experiments. ACS Earth Space Chem. 5 (4), 755–784.

Zhu, K., Sossi, P.A., Siebert, J., Moynier, F., 2019. Tracking the volatile and magmatic history of Vesta from chromium stable isotope variations in eucrite and diogenite meteorites. In: A GCA Special Volume in Honor of Professor Lawrence A. Taylor. Geochim. Cosmochim. Acta 266, 598–610. https://doi.org/10.1016/j.gca.2019.07.043.